Supplemental material for: Real-time exciton dynamics with time-dependent density-functional theory

Jiuyu Sun,[1,2] Cheng-Wei Lee,[3] Alina Kononov,[4] André Schleife,[3,5,6] and Carsten A. Ullrich[1]

[1] *Department of Physics and Astronomy, University of Missouri, Columbia, Missouri 65211, USA*
[2] *Max Planck Institute for the Structure and Dynamics of Matter, 22761 Hamburg, Germany*
[3] *Department of Materials Science and Engineering, University of Illinois at Urbana-Champaign, Urbana, Illinois 61801, USA*
[4] *Department of Physics, University of Illinois at Urbana-Champaign, Urbana, Illinois 61801, USA*
[5] *Materials Research Laboratory, University of Illinois at Urbana-Champaign, Urbana, Illinois 61801, USA*
[6] *National Center for Supercomputing Applications, University of Illinois at Urbana-Champaign, Urbana, Illinois 61801, USA*

(Dated: June 2, 2021)

I. CONSTRUCTING XC POTENTIALS FROM XC KERNELS

The time-dependent density can always be written as

$$n(\mathbf{r},t) = n_{\rm gs}(\mathbf{r}) + \delta n(\mathbf{r},t)\,, \tag{1}$$

i.e., as the sum of the ground-state density $n_{\rm gs}(\mathbf{r})$ and the density response $\delta n(\mathbf{r},t)$; the latter is not necessarily small compared to $n_{\rm gs}$. Likewise, one can write the time-dependent xc potential without restriction as

$$v_{\rm xc}[n](\mathbf{r},t) = v_{\rm xc}^{\rm gs}[n_{\rm gs}](\mathbf{r}) + v_{\rm xc}^{\rm dyn}[n](\mathbf{r},t)\,, \tag{2}$$

where $v_{\rm xc}^{\rm gs}$ is the ground-state xc potential (a functional of $n_{\rm gs}$ only), and the dynamical part $v_{\rm xc}^{\rm dyn}$ (a functional of the total n) is not necessarily small compared to $v_{\rm xc}^{\rm gs}$.

The time-dependent xc potential can be formally represented as a Taylor expansion around $n_{\rm gs}(\mathbf{r})$:

$$v_{\rm xc}[n](\mathbf{r},t) = v_{\rm xc}^{\rm gs}[n_{\rm gs}](\mathbf{r}) + \int dt' \int d\mathbf{r}' f_{\rm xc}[n_{\rm gs}](\mathbf{r},t,\mathbf{r}',t')\delta n(\mathbf{r}',t') \;+\; \ldots \tag{3}$$

where the xc kernel is defined as

$$f_{\rm xc}[n_{\rm gs}](\mathbf{r},t,\mathbf{r}',t') = \left.\frac{\delta v_{\rm xc}[n](\mathbf{r},t)}{\delta n(\mathbf{r}',t')}\right|_{n_{\rm gs}}\,. \tag{4}$$

The definition (4) tells us how to construct $f_{\rm xc}(\mathbf{r},t,\mathbf{r}',t')$ from a given $v_{\rm xc}(\mathbf{r},t)$ via a functional derivative.

But suppose we start from a certain model expression $f_{\rm xc}^{\rm model}$ for the xc kernel and ask whether one can write this as a functional derivative of a model xc potential, i.e.,

$$f_{\rm xc}^{\rm model}[n_{\rm gs}](\mathbf{r},t,\mathbf{r}',t') \stackrel{?}{=} \left.\frac{\delta v_{\rm xc}^{\rm model}[n](\mathbf{r},t)}{\delta n(\mathbf{r}',t')}\right|_{n_{\rm gs}}\,. \tag{5}$$

The answer, in general, is no: there is no guarantee that a model xc kernel can be written as a functional derivative [1]. In other words, a matching $v_{\rm xc}^{\rm model}[n](\mathbf{r},t)$ may not exist. In that case, the best we can do is to construct an approximation for the dynamical part of the xc potential:

$$v_{\rm xc}^{\rm dyn,model}(\mathbf{r},t) \approx \int dt' \int d\mathbf{r}' f_{\rm xc}^{\rm model}(\mathbf{r},t,\mathbf{r}',t')\delta n(\mathbf{r}',t')\,, \tag{6}$$

which is valid in the weakly perturbed limit where $|\delta n(\mathbf{r},t)| \ll n_{\rm gs}(\mathbf{r})$. Beyond that limit, Eq. (6) becomes in general an uncontrolled approximation.

A special case is the LRC xc kernel

$$f_{\rm xc}^{\rm LRC}(\mathbf{r},t,\mathbf{r}',t') = -\frac{\alpha}{4\pi}\frac{\delta(t-t')}{|\mathbf{r}-\mathbf{r}'|}\,, \tag{7}$$

which is nothing but the Hartree kernel multiplied by the constant $-\alpha/4\pi$. Treating α as a fixed parameter, it is straightforward to express the LRC kernel as a functional derivative, namely,

$$f_{\rm xc}^{\rm LRC,fixed}(\mathbf{r},t,\mathbf{r}',t') = \left.\frac{\delta v_{\rm xc}^{\rm LRC,fixed}(\mathbf{r},t)}{\delta n(\mathbf{r}',t')}\right|_{n_{\rm gs}} \tag{8}$$

where

$$v_{\rm xc}^{\rm LRC,fixed}(\mathbf{r},t) = -\frac{\alpha}{4\pi}\int d\mathbf{r}'\frac{n(\mathbf{r}',t)}{|\mathbf{r}-\mathbf{r}'|}\,. \tag{9}$$

Notice that here the Taylor expansion (3) terminates rigorously after the linear term.

However, in reality the parameter α is not fixed but material-dependent, which makes it formally an implicit (unknown) functional of the density. Expression (9) is only valid under the assumption that the functional derivative $\delta\alpha/\delta n$ is zero. Thus, again, the best we can do is to restrict ourselves to the dynamical part of the xc potential using the approximation (6). The result is

$$v_{\rm xc}^{\rm dyn,LRC}(\mathbf{r},t) = -\frac{\alpha}{4\pi}\int d\mathbf{r}'\frac{\delta n(\mathbf{r}',t)}{|\mathbf{r}-\mathbf{r}'|}\,, \tag{10}$$

which is what we use in the main paper.

To summarize: we can approximately reconstruct an xc potential from any xc kernel, but this is formally limited to the weakly perturbed regime, and we only obtain an expression for the dynamical part $v_{\rm xc}^{\rm dyn}(\mathbf{r},t)$. The corresponding $v_{\rm xc}^{\rm gs}(\mathbf{r})$ remains undetermined.

It is tempting to use the approximate $v_{\rm xc}^{\rm dyn}(\mathbf{r},t)$ beyond the realm for which it is designed to be valid, i.e., if $\delta n(\mathbf{r},t)$ is no longer small. Extending approximations in this way has a long tradition in (TD)DFT [a prime example is the (A)LDA], but, as always, one should proceed with some caution.

II. REMARKS ABOUT LRC AND LRC$_+$

A. Implementation of the scaled ALDA

In the main paper, we define three types of exchange-correlation (xc) kernels: adiabatic LDA ($f_{\rm xc}^{\rm ALDA}$), long-range corrected (LRC) ($f_{\rm xc}^{\rm LRC}$), and the combined kernel $f_{\rm xc}^{\rm LRC+} = f_{\rm xc}^{\rm LRC} + \beta f_{\rm xc}^{\rm ALDA}$. Within linear-response (LR)-TDDFT, the implementation of these xc kernels is straightforward in the Yambo code [2]. However, in real-time (RT)-TDDFT using Qb@ll [3–5], the implementation of the β-scaled ALDA needs to be done with care, to ensure that the LR and RT formalisms are consistent.

The default implementation of the ALDA in Qb@ll involves the full xc potential $v_{\rm xc}^{\rm ALDA}[n](t)$, but the β-scaling only affects the response part associated with $\delta n(t)$ [in the main paper, we define $n(\mathbf{r},t) = n_{\rm gs}(\mathbf{r}) + \delta n(\mathbf{r},t)$, where the density response $\delta n(\mathbf{r},t)$ is not necessarily small compared to the lattice-periodic $n_{\rm gs}(\mathbf{r})$]. Let us consider the fundamental relationship $f_{\rm xc}^{\rm ALDA}(\mathbf{r},\mathbf{r}') = \delta v_{\rm xc}^{\rm LDA}[n](\mathbf{r})/\delta n(\mathbf{r}')\big|_{n_{\rm gs}(\mathbf{r})}$. Multiplying β on both sides, we have

$$\beta f_{\rm xc}^{\rm ALDA}(\mathbf{r},\mathbf{r}') = \left.\frac{\beta\delta v_{\rm xc}^{\rm LDA}[n](\mathbf{r})}{\delta n(\mathbf{r}')}\right|_{n_{\rm gs}(\mathbf{r})} . \qquad (11)$$

This suggests the algorithm for RT-TDDFT with the β-scaled ALDA xc potential, $v_{{\rm xc},\beta}^{\rm ALDA}$, described in the following pseudocode, where $\Psi(t)$ denotes the Kohn-Sham wave function:

Algorithm 1 β-scaled ALDA xc potential

Require: ground state $v_{\rm xc}^{\rm LDA}$, $\Psi(0) = \Psi_{\rm gs}$

  for $istep = 1 \to nsteps$ **do**

    generate $n(t)$ from $\Psi(t)$

    update $v_{\rm xc}^{\rm ALDA}[n](t)$ with $n(t)$

    $\beta\delta v_{\rm xc}^{\rm ALDA}(t) = \beta[v_{\rm xc}^{\rm ALDA}[n](t) - v_{\rm xc}^{\rm LDA}]$

    $v_{{\rm xc},\beta}^{\rm ALDA}(t) = v_{\rm xc}^{\rm LDA} + \beta\delta v_{\rm xc}^{\rm ALDA}(t)$

    propagate $\Psi(t) \to \Psi(t+\Delta t)$ with $v_{{\rm xc},\beta}^{\rm ALDA}(t)$

    $t = t + \Delta t$

  end for

Notice that the parameter β can be set to zero, in which case $f_{\rm xc}^{\rm LRC+}$ reduces to the pure LRC kernel $f_{\rm xc}^{\rm LRC} = -\alpha/k^2$, and there are no dynamical corrections to the ground-state LDA xc potential; this is used for the H_2 chain in the main paper.

B. Choice of α and β

The scaling factors α and β are introduced here as empirical parameters. The parameter α could, in principle, be determined from first principles, since the LRC kernel (7) is designed to mimick the exact long-range behavior of the xc kernel, $f_{{\rm xc},\mathbf{G}=0,\mathbf{G}'=0}(\mathbf{k}\to 0,\omega) \to \kappa_{00}/k^2$ where, formally, κ_{00} is frequency-dependent and a functional of the density. α could also be determined using the semiempirical scaling approach of Ref. [6], or even by fitting of experimental or BSE spectra. Likewise, β could conceivably be optimized via fitting.

In practice, we always started with $\beta = 1$ (i.e., pure ALDA), and then determined α via LR-TDDFT, comparing with experimental or BSE optical spectra. In the case of Si and LiF, we had some guidance through earlier work [6], for H_2 and $CsGeCl_3$ a bit of trial and error was involved. We then used the so determined α in RT-TDDFT. If instabilities in the current oscillations were detected, we gradually reduced α and increased β until the time propagation was sufficiently stable.

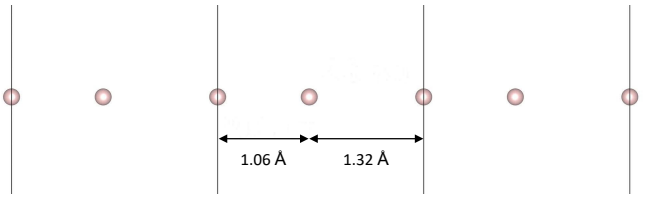

FIG. 1. Geometry of the molecular H_2 chain, with lattice constant 2.38 Å.

III. COMPUTATIONAL DETAILS

A. Real-time propagation with Qb@ll

1. *Geometries and implementation*

Since it is more convenient to adopt an orthogonal unit cell in Qb@ll, we used a conventional cubic cell containing 8 Si atoms for Si and 4 Li and 4 F atoms for LiF, respectively, with the experimental lattice parameters. The H_2 chain is set up to have a lattice constant of 2.38 Å along the periodic direction (see Fig. 1). For $CsGeCl_3$, we adopted the cubic $Pm\bar{3}m$ phase. The lattice constant is optimized (using the Quantum Espresso package [7], see below) to be 5.46 Å, which is in agreement with results quoted in the literature [8].

With the geometries as defined above, we first calculate the Kohn-Sham ground state for all systems. A plane wave basis implementation (the default in Qb@ll) is employed, with cutoff energies of 20 Hartree for Si and 40 Hartree for the other three systems. Together with optimized norm-conserving Vanderbilt pseudopotentials [9, 10], we used the LDA functional for Si, H_2 chain and LiF, and the PBE [11] functional for $CsGeCl_3$. We used regular Monkhorst-Pack (M-P) meshes of $64\times1\times1$, $6\times6\times6$ and $8\times8\times8$ for H_2 chain, LiF and $CsGeCl_3$, respectively. The $\mathbf{k}$-point meshes adopted for Si will be discussed in more detail in Section IV below.

2. Excitation mechanism and observables

Starting from the ground state, the systems are excited in two different ways for the linear response and short-pulse response simulations, respectively. In the velocity gauge, see Eq. (4) in the main paper, a uniform external electric field $\mathbf{E}'$ gives rise to a vector potential $\mathbf{A}'(t)$,

$$\mathbf{A}'(t) = -\int^t \mathbf{E}'(t')dt' \,, \tag{12}$$

and the single-particle Bloch functions acquire a phase factor when going from the length to the velocity gauge:

$$\varphi_j(\mathbf{r},t) = e^{-i\mathbf{A}'\cdot\mathbf{r}}\tilde{\varphi}_j(\mathbf{r},t) \,. \tag{13}$$

For our calculations in the weakly perturbed regime (to obtain optical spectra for comparison with LR-TDDFT), we adopted a delta-kick by a constant and uniform electric field $\mathbf{E}'$ along the z-direction. This means that a constant $\mathbf{A}'$ along the z-direction is turned on at the beginning of the propagation, i.e. $\mathbf{A}'(t) = const.$ $(t \geq 0)$. We chose small values of $\mathbf{A}'$ of 5×10^{-3} a.u. for Si, H_2 chain and $CsGeCl_3$, and 5×10^{-4} a.u. for LiF (which corresponds to electric field spikes of strength 2.6 and 0.26 V/nm, respectively). Our specific choice of pulse shapes for the short-pulse response simulations is discussed in the main paper.

With the accumulated macroscopic total current density $\mathbf{j_0}$ of every step, the dielectric response $\varepsilon(\omega)$ is calculated via [12]

$$\varepsilon(\omega) = 1 + \frac{4\pi i\sigma(\omega)}{\omega} \,, \tag{14}$$

where the frequency-dependent conductivity is given by

$$\sigma(\omega) = -\frac{1}{A'}\int^T e^{i\omega t} f(t) j_{\mathbf{0}}(t) dt, \tag{15}$$

and $f(t)$ is a suitably chosen window function (here, we use a third-order polynomial). In order to compare with experimental or BSE results, the dielectric functions are corrected by rigid blue shifts of 0.6 eV, 3.05 eV, 5.4 eV and 1.6 eV for Si, H_2 chain, LiF and $CsGeCl_3$, respectively.

For the nonlinear short-pulse response in Si, see Fig. 2 in the main paper, we used the same **k**-grid as before. Instead of calculating the dielectric function and applying the scissors operator, we follow Ref. [13] and consider the dipole power spectrum (in the so-called acceleration form), following from the time-dependent induced current:

$$|P(\omega)|^2 = \left| FT \int_\Omega d\mathbf{r} \frac{\partial}{\partial t}\mathbf{j}(\mathbf{r},t) \right|^2 \tag{16}$$

where FT stands for Fourier Transform. The dipole power spectrum has been widely used to study harmonic generation in atoms, molecules and, more recently, solids.

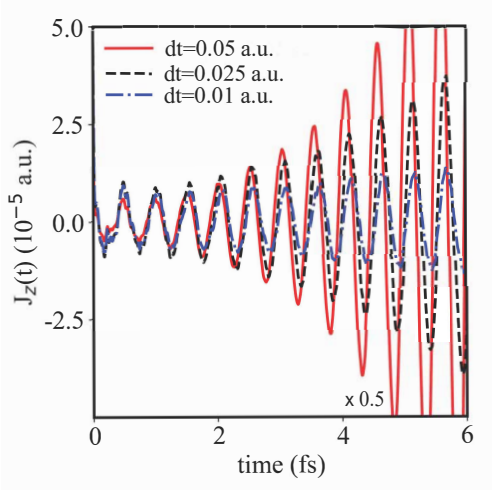

FIG. 2. Macroscopic induced current $J_z(t)$ of LiF, calculated with Qb@ll using different time steps $dt = 0.05$ a.u. (1.21 as), $dt = 0.025$ a.u. (0.605 as), and $dt = 0.01$ a.u. (0.242 as). The method used is LRC_+ with $\alpha = 7$ and $\beta = 1$.

3. Numerical time propagation

For the time propagation we use a fourth-order Runge-Kutta algorithm [14]. A time step of 1.93 attoseconds (as) is employed for Si, a time step of 1.21 as for the H_2 chain and for $CsGeCl_3$, and a time step of 0.605 as for LiF. A time propagation of at least 20 fs is performed for all the systems unless the simulation diverges.

In materials with strongly bound excitons, instabilities may occur due to the violation of the zero-force theorem, as discussed in the main paper. These instabilities manifest through current oscillations with increasing amplitude (without any external driving forces). However, the numerical details of the time propagation can play a significant role, as illustrated in Fig. 2. Clearly, the instabilities for LiF are worse for longer time steps; for smaller time steps, the instabilities build up more slowly, but eventually the current oscillations blow up as well. In practice, we chose the time step $dt = 0.025$ a.u. (0.605 as) for LiF as the best compromise between stability and overall computational cost (except for the stable case with $\alpha = 10^{-4}$ and $\beta = 6.4$, where we can use $dt = 1.21$ as).

B. Optical response with Yambo

We used the Yambo code [2] to perform LR-TDDFT and BSE calculations for optical excitations. The Kohn-Sham ground-state wave functions, used as input to Yambo, are calculated using the Quantum Espresso package [7]. Except for the **k**-point mesh, we apply the same cubic cells and computational parameters, as well as the scissors operator, to remain consistent with Qb@ll. For the ground state and LR-TDDFT, we used Γ-centered

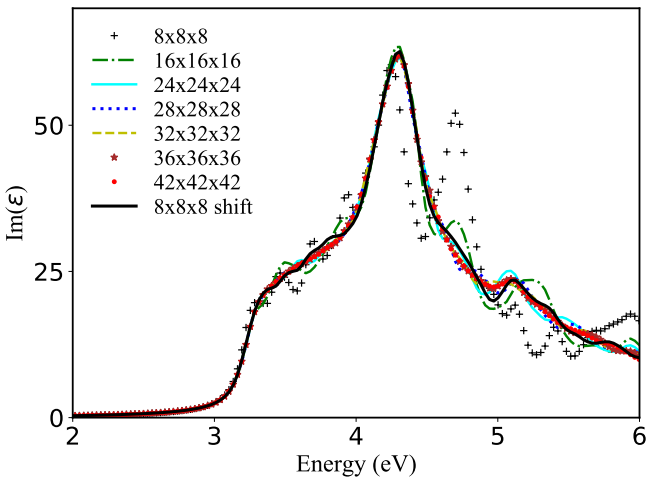

FIG. 3. RPA dielectric function Im(ε) of Si calculated using different **k**-point meshes with Quantum Espresso. A scissors shift of 0.6 eV is applied.

meshes of $64 \times 1 \times 1$, $8 \times 8 \times 8$ and $12 \times 12 \times 12$ for H_2 chain, LiF and $CsGeCl_3$, respectively.

The RPA dielectric functions were calculated with at least 100 conduction bands and 123 **G**-vectors for Si. The corresponding numbers for the other materials are: 19 conduction bands and 1005 **G**-vectors for the H_2 chain, 160 conduction bands and 200 **G**-vectors for LiF, and 160 conduction bands and 300 **G**-vectors for $CsGeCl_3$. For our LR-TDDFT calculations, these parameters are kept the same as for the RPA calculations for each material, except we only use 1 conduction band for the H_2 chain.

To build the BSE kernels, we used 4 valence and 4 conduction bands for Si. The corresponding numbers of valence and conduction bands for the other materials are: (1,1) for the H_2 chain and (13,7) for $CsGeCl_3$. We used Haydock iteration [15, 16] to solve the BSE-type equations, instead of directly diagonalizing the huge BSE matrix.

Due to the absence of experimental data for the electronic band gap of H_2 chain and cubic $CsGeCl_3$, we used the G_0W_0 method to correct the quasiparticle energy. With the RPA dielectric function obtained above, we included 32 and 160 conduction bands for H_2 chain and $CsGeCl_3$, respectively. The band gap correction for the H_2 chain is 3.05 eV, which is applied as the magnitude of scissors shift in BSE. The BSE optical spectrum is in agreement with Ref. [17]. Thus we further applied this scissors shift for LR-TDDFT. The electronic band gap of cubic $CsGeCl_3$ is corrected to be 2.96 eV, which is in agreement with previous work [8]. Thus a correction of 1.6 eV is then applied as a scissors shift for all optical spectra of $CsGeCl_3$ with BSE and LR-TDDFT. Note here that the scissors shift is different from the rigid shift applied in RT-TDDFT [18, 19], though we adopted the same value for each material.

For the H_2 chain, we encountered some numerical difficulties with Yambo when we tried to combine LRC with a β-scaled ALDA (i.e., LRC_+). These difficulties point to an enhanced sensitivity of the ALDA kernel in quasi-1D. Therefore, we used the pure LRC kernel only for the H_2 chain (see also [20]).

C. Computational cost

For the materials considered here, the computational cost to obtain optical spectra was lower using LR-TDDFT (Yambo) compared to RT-TDDFT (Qb@ll), but these two codes have very different numerical implementations, so a direct comparison of the cost of LR- and RT-TDDFT is not very meaningful. Qb@ll's main strength is for systems with very large unit cells (or supercells), and less so for the relatively simple systems with small unit cells considered here. In general, RT-TDDFT scales favorably with system size compared to LR-TDDFT, and it parallelizes more easily. Another important factor are the memory requirements: again, RT calculations will have the advantage over LR for large systems, since it is not necessary to include unoccupied states.

IV. MORE ON k-POINT SAMPLING

A. k-point sampling for TDDFT

We carefully tested the **k**-point sampling for calculating the dielectric function Im(ε) of Si (with an 8-atom unit cell). The calculations were performed with the Quantum Espresso package by using *pw.x* and *epsilon.x*, where the RPA level was constructed using Kohn-Sham ground-state wave functions. As shown in Fig. 3, we tested M-P **k**-point meshes [21] from 8^3 up to 42^3. It can be seen that Im(ε) is not well converged until the **k**-point mesh of 28^3 for the lower energy part below 4 eV. However, the higher energy part beyond 5.5 eV is still not converged even when the number of **k**-points increases from 36^3 to 42^3.

It has been reported in the literature that RT-TDDFT simulations can be sensitive to **k**-point sampling [12]. In order to reduce the computational cost and keep the **k**-point sampling still adequate, we applied an additional shift based on the 8^3 M-P mesh. This random shift breaks the symmetries that are inherent to the otherwise regular **k**-point grid, since Qb@ll does not employ symmetry reduction of the supplied grid. Hence, it is ideal if a grid of a given size has as few symmetry-equivalent **k**-points in it as possible, and we approximate this with a random shift of the entire mesh. The additional small shift by the reciprocal-space vector $\boldsymbol{v} = (0.028526, 0.041304, 0.107901)$ is randomly generated. Then we applied the same random shift vector to every **k**-point of the 8^3 M-P mesh. With the shifted 8^3 mesh, we obtained a curve of Im(ε) (black solid line) similarly smooth as that with the 28^3 mesh (blue dotted

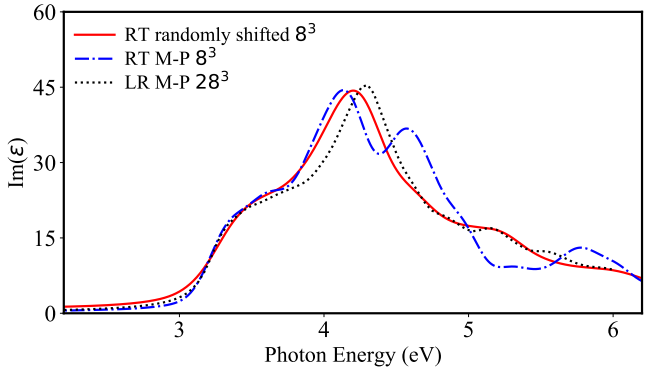

FIG. 4. Dielectric function Im(ε) of Si calculated by RT ALDA with different 8^3 **k**-meshes, as well as LR ALDA with 8^3 M-P mesh. A scissors shift of 0.6 eV is applied.

line). Therefore, in the main paper we use this shifted 8^3 mesh for all the RT simulations of Si with Qb@ll.

However, randomly shifted meshes are unavailable in the Yambo code, where we have to use a Γ-centered or M-P mesh. Based on the results above, we choose an M-P mesh of 28^3 for the LR-TDDFT calculations in Yambo. We compare Im(ε) of Si calculated with different meshes in Fig. 4. For RT-TDDFT, the ALDA spectrum with the randomly shifted mesh is much improved compared to that calculated with a regular M-P mesh, especially for eliminating the artificial peak around 4.6 eV. In fact, RT-TDDFT with the randomly shifted mesh is similar to LR-TDDFT with the 28^3 mesh, which confirms our conclusions from the test above with Quantum Espresso.

The slight differences between the LR- and RT-TDDFT optical spectra of Si in Figs. 1 in the main paper can be mainly attributed to the use of different **k**-meshes. Even though we obtained almost identical RPA results for the randomly shifted 8^3 mesh and the 28^3 M-P mesh, there is no guarantee that these two meshes work similarly for different TDDFT approaches. This is particularly evident in the LRC$_+$ optical spectra of Si, where LR- and RT-TDDFT give overall similar results, but the E_1 and E_2 peaks are not quite aligned.

B. k-point sampling for BSE

The M-P mesh of 28^3 gives well converged spectra, but we cannot use it for BSE calculations because of the huge cost for a unit cell containing 8 Si atoms. It is well known that a large number of **k**-points, even much more than 28^3, are required to obtain converged BSE spectra [22, 23]. We adopted the random integration method and inversion solver in Yambo [2, 24]. In this scheme, the BSE spectrum of Si is calculated with a double **k**-grid, which includes a $24 \times 24 \times 24$ Γ-centered uniform **k**-point mesh and 30000 random interpolated **k**-points. In addition, we chose to use a primitive cell with 2 Si atoms for BSE calculations.

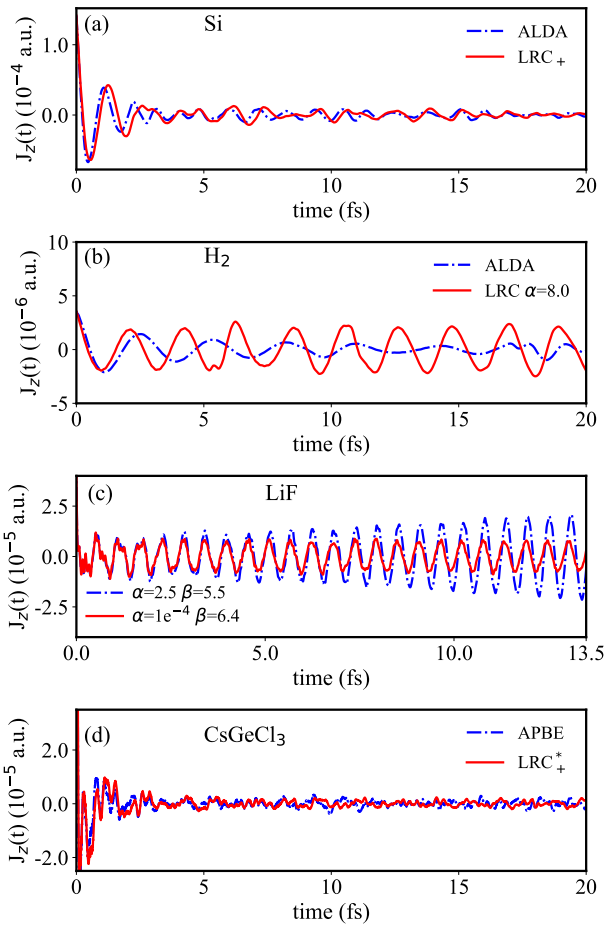

FIG. 5. Real-time current densities J_z calculated by RT-TDDFT for the linear dielectric response of (a) Si, (b) H_2 chain, (c) LiF and (d) $CsGeCl_3$.

In Fig. 1 in the main paper, it is found that the BSE spectrum differs from the experiment by a lower E_1 peak. At this stage, increasing the number of **k**-points would be unlikely to improve the result. Other factors should be taken into account, for example dynamical effects in the screened electron-hole interaction, as discussed in detail in Ref. [25].

For $CsGeCl_3$, we also applied the double **k**-grid technique, using a Γ-centered 8^3 uniform **k**-mesh and 10000 random interpolated **k**-points. For the H_2 chain, we used the same **k**-mesh of $64 \times 1 \times 1$ as in LR-TDDFT (see Sec. III.B).

V. REAL-TIME CURRENT DENSITIES FOR Si, H_2 CHAIN AND LiF

In this section, we present the real-time total current densities (J_z) of Si, H_2 chain, LiF, and $CsGeCl_3$, which are not shown in the main paper (Si, $CsGeCl_3$) or only

shown for a shorter time (H_2, LiF). All results here are for weak excitation by a delta-kicked electric field, see Sec. III.A.2 above (for Si, the currents induced by femtosecond laser pulses are shown in Fig. 2a in the main paper).

In Fig. 5a, we compare the macroscopic J_z of Si generated by ALDA and LRC_+ in the main paper. It can be seen that the oscillations of both current densities become much smaller after a time propagation of 20 fs. This is due to the fact that the exciton in Si is close to the conduction band continuum, which leads to a rather rapid dephasing of the induced current oscillations.

By contrast, in Fig. 5b for the H_2 chain, the J_z generated by LRC with $\alpha = 8.0$ exhibits a much stronger oscillation than J_z by ALDA, even no trend of decay. In the one-dimensional hydrogen chain, the exciton is strongly bound and has a large oscillator strength, which is reflected by the prominent oscillations in the current density.

In LiF, the frequencies of the current oscillations by LRC_+ with $(\alpha = 2.5, \beta = 5.5)$ and $(\alpha = 10^{-4}, \beta = 6.4)$ are almost the same, which gives us the excitonic peaks so close to each other in energy (see Fig. 3c in the main paper). However, the oscillations of J_z for $(\alpha = 2.5, \beta = 5.5)$ remain strong after 5 fs, which leads to a much higher peak in the optical spectrum. In addition, one can also observe an instability of the induced currents for $(\alpha = 2.5, \beta = 5.5)$.

For $CsGeCl_3$, the induced current densities are quite similar to those for Si discussed above, which is related to the fact that both systems have weakly bound excitons, close to or even partially embedded into the absorption continuum.

[1] A. P. Gaiduk and V. N. Staroverov, How to tell when a model Kohn-Sham potential is not a functional derivative, J. Chem. Phys. **131**, 044107 (2009).

[2] D. Sangalli, A. Ferretti, H. Miranda, C. Attaccalite, I. Marri, E. Cannuccia, P. Melo, M. Marsili, F. Paleari, A. Marrazzo, G. Prandini, P. Bonfà, M. O. Atambo, F. Affinito, M. Palummo, A. Molina-Sánchez, C. Hogan, M. Grüning, D. Varsano, and A. Marini, Many-body perturbation theory calculations using the yambo code, J. Phys.: Condens. Matter **31**, 325902 (2019).

[3] E. W. Draeger and F. Gygi, Qbox code, qb@ll version, `https://github.com/LLNL/qball` (2017), Lawrence Livermore National Laboratory.

[4] A. Schleife, E. W. Draeger, V. M. Anisimov, A. A. Correa, and Y. Kanai, Quantum dynamics simulation of electrons in materials on high-performance computers, Comput. Sci. Eng. **16**, 54 (2014).

[5] E. Draeger, X. Andrade, J. Gunnels, A. Bhatele, A. Schleife, and A. Correa, Massively parallel first-principles simulation of electron dynamics in materials, J. Parallel Distrib. Comput. **106**, 205 (2017).

[6] Y.-M. Byun and C. A. Ullrich, Assessment of long-range-corrected exchange-correlation kernels for solids: Accurate exciton binding energies via an empirically scaled bootstrap kernel, Phys. Rev. B **95**, 205136 (2017).

[7] P. Giannozzi, O. Andreussi, T. Brumme, O. Bunau, M. B. Nardelli, M. Calandra, R. Car, C. Cavazzoni, D. Ceresoli, M. Cococcioni, N. Colonna, I. Carnimeo, A. D. Corso, S. de Gironcoli, P. Delugas, R. A. D. Jr, A. Ferretti, A. Floris, G. Fratesi, G. Fugallo, R. Gebauer, U. Gerstmann, F. Giustino, T. Gorni, J. Jia, M. Kawamura, H.-Y. Ko, A. Kokalj, E. Küçükbenli, M. Lazzeri, M. Marsili, N. Marzari, F. Mauri, N. L. Nguyen, H.-V. Nguyen, A. O. de-la Roza, L. Paulatto, S. Poncé, D. Rocca, R. Sabatini, B. Santra, M. Schlipf, A. P. Seitsonen, A. Smogunov, I. Timrov, T. Thonhauser, P. Umari, N. Vast, X. Wu, and S. Baroni, Advanced capabilities for materials modelling with QUANTUM ESPRESSO, J. Phys.: Condens. Matter **29**, 465901 (2017).

[8] L.-y. Huang and W. R. L. Lambrecht, Electronic band structure trends of perovskite halides: Beyond Pb and Sn to Ge and Si, Phys. Rev. B **93**, 195211 (2016).

[9] D. R. Hamann, Optimized norm-conserving Vanderbilt pseudopotentials, Phys. Rev. B **88**, 085117 (2013), erratum: *ibid.* **95**, 239906 (2017).

[10] M. van Setten, M. Giantomassi, E. Bousquet, M. Verstraete, D. Hamann, X. Gonze, and G.-M. Rignanese, The pseudodojo: Training and grading a 85 element optimized norm-conserving pseudopotential table, Comput. Phys. Commun. **226**, 39 (2018).

[11] J. P. Perdew, K. Burke, and M. Ernzerhof, Generalized gradient approximation made simple, Phys. Rev. Lett. **77**, 3865 (1996), erratum: *ibid.* **78**, 1396 (1997).

[12] K. Yabana, T. Sugiyama, Y. Shinohara, T. Otobe, and G. F. Bertsch, Time-dependent density functional theory for strong electromagnetic fields in crystalline solids, Phys. Rev. B **85**, 045134 (2012).

[13] N. Tancogne-Dejean, O. D. Mücke, F. X. Kärtner, and A. Rubio, Impact of the electronic band structure in high-harmonic generation spectra of solids, Phys. Rev. Lett. **118**, 087403 (2017).

[14] A. Schleife, E. W. Draeger, Y. Kanai, and A. A. Correa, Plane-wave pseudopotential implementation of explicit integrators for time-dependent Kohn-Sham equations in large-scale simulations, J. Chem. Phys. **137**, 22A546 (2012).

[15] R. Haydock, The recursive solution of the Schrödinger equation, Comput. Phys. Commun. **20**, 11 (1980).

[16] L. X. Benedict and E. L. Shirley, Ab initio calculation of $\epsilon_2(\omega)$ including the electron-hole interaction: Application to GaN and CaF_2, Phys. Rev. B **59**, 5441 (1999).

[17] D. Varsano, A. Marini, and A. Rubio, Optical saturation driven by exciton confinement in molecular chains: A time-dependent density-functional theory approach, Phys. Rev. Lett. **101**, 133002 (2008).

[18] Z. H. Levine and D. C. Allan, Linear optical response in silicon and germanium including self-energy effects, Phys. Rev. Lett. **63**, 1719 (1989).

[19] X. Gonze and C. Lee, Dynamical matrices, Born effective charges, dielectric permittivity tensors, and interatomic force constants from density-functional perturbation theory, Phys. Rev. B **55**, 10355 (1997).

[20] See the Yambo tutorial at http://www.yambo-code.org/wiki/index.php?title=Hydrogen_chain.
[21] H. J. Monkhorst and J. D. Pack, Special points for Brillouin-zone integrations, Phys. Rev. B **13**, 5188 (1976).
[22] D. Rocca, Y. Ping, R. Gebauer, and G. Galli, Solution of the Bethe-Salpeter equation without empty electronic states: Application to the absorption spectra of bulk systems, Phys. Rev. B **85**, 045116 (2012).
[23] S. Albrecht, L. Reining, G. Onida, V. Olevano, and R. Del Sole, Albrecht et al. reply:, Phys. Rev. Lett. **83**, 3971 (1999).
[24] D. Kammerlander, S. Botti, M. A. L. Marques, A. Marini, and C. Attaccalite, Speeding up the solution of the Bethe-Salpeter equation by a double-grid method and Wannier interpolation, Phys. Rev. B **86**, 125203 (2012).
[25] A. Marini and R. Del Sole, Dynamical excitonic effects in metals and semiconductors, Phys. Rev. Lett. **91**, 176402 (2003).